KERNFORSCHUNGSANLAGE JÜLICH GmbH
Institut für Reaktorentwicklung

A MEDIUM ENERGY NEUTRON DEEP PENETRATION EXPERIMENT

– EXPERIMENTAL AND THEORETICAL ANALYSIS –

by

W. Amian, P. Cloth, V. Drüke, D. Filges,
N. Paul, H. Schaal

Jül-2101
November 1986
ISSN 0366-0885

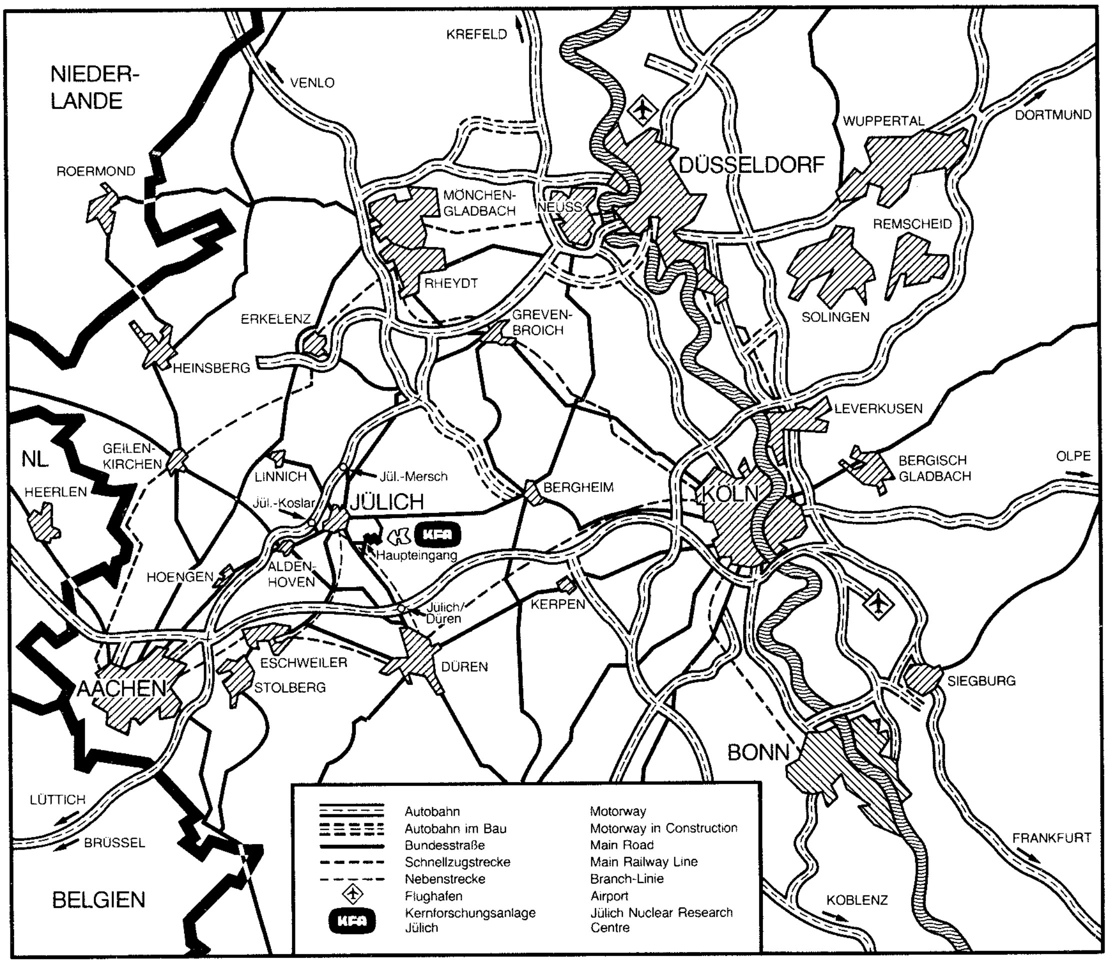

Als Manuskript gedruckt

Berichte der Kernforschungsanlage Jülich – Nr. 2101
Institut für Reaktorentwicklung Jül-2101

Zu beziehen durch: ZENTRALBIBLIOTHEK der Kernforschungsanlage Jülich GmbH
Postfach 1913 · D-5170 Jülich (Bundesrepublik Deutschland)
Telefon: 02461/610 · Telex: 833556-0 kf d

A MEDIUM ENERGY NEUTRON DEEP PENETRATION EXPERIMENT

– EXPERIMENTAL AND THEORETICAL ANALYSIS –

by

W. Amian, P. Cloth, V. Drüke, D. Filges,
N. Paul, H. Schaal

A Medium Energy Neutron Deep Penetration Experiment
- Experimental and Theoretical Analysis -

by

W. Amian, P. Cloth, V. Drüke, D. Filges, N. Paul,
H. Schaal

Abstract

A deep penetration experiment conducted at the Los Alamos WNR facility's Spallation Neutron Target is compared with calculations using intra-nuclear-cascade and S_N-transport codes installed at KFA-IRE. In the experiment medium energy reactions induced by neutrons between 15 MeV and about 150 MeV inside a quasi infinite slab of iron have been measured using copper foil monitors. Details of the experimental prodedure and the theoretical methods are described. A comparison of absolute reaction rates for both experimentally and theoretically derived reactions is given. The present knowledge of the corresponding monitor reaction cross sections is discussed.

Contents

I. INTRODUCTION

In this paper we report on a deep penetration experiment conducted at the Los Alamos WNR facility's Spallation Neutron Target /1/. The experiments are compared with calculations to help validating those features of the present HETC/KFA-1 /2/, and ANISN /3/ codes installed at KFA-IRE which are applied to deep penetration problems for high-energy neutrons above 15 MeV.

For such problems the most reasonable technique to detect neutrons is by counting decaying residual nuclei of high energy interactions with suitable target materials. Especially for accelerator environments, spallation reactions on copper have been proposed by Routti /4/ as a means to extend the known threshold-foil technique to higher hadron energies. The yield cross sections for many spallation products have a threshold type energy dependence with threshold energies of tens or hundreds of MeV. The advantage of these spallation detectors is that several gamma-active products with different threshold energies can be obtained from only one measurement.

The problem with these reactions, however, is that the spallation yield cross sections are uncertain above 20 MeV.
While the experiments can reveal clearly the exponential decrease of reaction rates with shielding thickness without any prior knowledge of cross sections, the quantitative comparison between experiment and calculation suffers from the lack of reliable cross section data for these spallation yield cross sections.

We will demonstrate this deficiency by a comparison of experimentally and theoretically determined production cross sections for some isotopes from natural copper.

II. EXPERIMENTAL PROCEDURE

Foils of 30 mm diameter and 1 mm thickness were irradiated inside the WNR target 1 bulk shield. They were imbedded into a stringer assembly that was inserted into flight path 5 of the facility. Foil materials inserted were aluminum, copper, iron, indium, cobalt, zirconium, niobium and nickel, all of natural isotopic composition. The stringer assembly loaded with iron foil containers and part of the WNR bulk shield are shown in Figure 1 and Figure 2, respectively. Flight path 5 was filled with massive iron rings as indicated in Figure 2, and vacuum sealed against the environment by an inner and outer vacuum pipe. This enabled the experimentalist to insert and remove the central iron tube - the so called "stringer" - within minutes during a run cycle while the beam was off for only a few minutes.

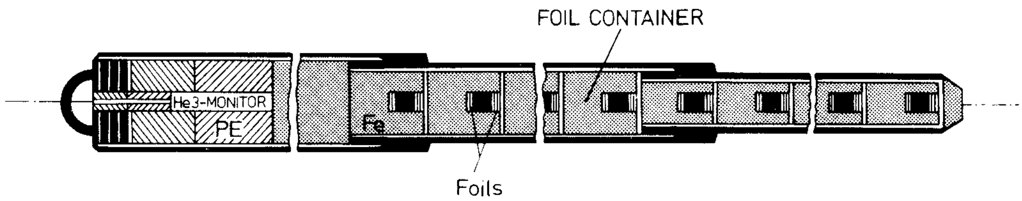

Fig. 1: The stringer assembly used to insert foil packages into the bulk shield of the WNR facility's Target I (LANSCE). Individual foil containers and foil positions are indicated. The ^{3}He monitor at the left is imbedded into PE rings and serves as a flux monitor.

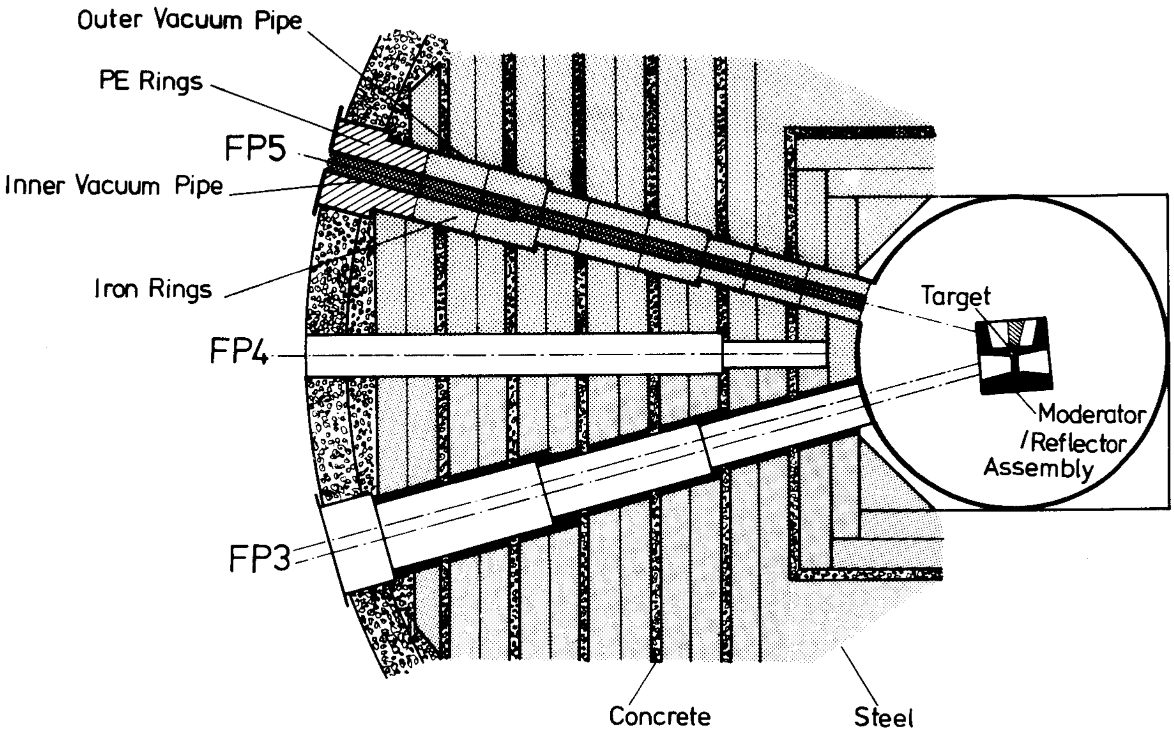

Fig. 2: Schematic sketch of the WNR target to the south. The stringer of Fig. 1 was inserted into Flight Path 5 (FP 5) for irradiations. Target, moderator and reflector are described in more detail in /1/

During irradiations, ^{3}He-detector counts were recorded to correct for time variations of the proton-beam intensity and the resulting neutron-flux intensity. The ^{3}He detector was positioned in a polyethylene cylinder at the flight path's end (Fig. 1). This position was chosen to prevent interference from neighbouring experiments.

Most irradiations were performed with a tungsten target (4.45 cm diameter, 24 cm length) and a beryllium reflected water moderator assembly in place. Only one run (run 3) was with a bare tantalum target (2.54 cm diameter, 15 cm length) buth with only one tenth in beam intensity. The mean beam currents are given in Table I. They were derived from the recorded ^{3}He-detector counts per timestep and a given value of 4 μA beam current during a time period towards the end of the second run. From these numbers a conversion factor of 4.83x10^{10} protons per monitor count was derived. The error of this calibration was estimated to be less than 10 percent.

Table I: Characteristics of the seven runs. All but run 3 have been done under the same beam conditions and for the same target configuration; see text for more details. The beam currents have been derived from the neutron monitor counts and a conversion factor of 4.83x10^{10} protons per monitor count

Run	Length (hrs.)	Beam Current (μA)	Beam off Time (percent)
1	260.1	2.55	13.6
2	157.7	3.41	5.1
3	159.7	0.21	10.9
4	206.0	2.84	23.1
5	116.2	3.37	10.0
6	2.52	3.75	3.3
7	140.1	3.02	4.5

The 4 μA value for the beam current is a value recorded far upstream from the target. Downstream this monitor position the beam is transported through the beam line and bent down to the target. By maximizing the target's temperature it was made sure that the beam was approximately centered on target. Without major beam losses the given value should be very close to the actual value on target. However, beam losses by not focussing the beam exactly on target cannot be excluded. With the upgrade of the WNR facility this problem will be solved.

After irradiations the reaction products in all foils were determined directly by counting in Ge(Li) gamma-ray spectrometers. The Ge(Li) detectors were calibrated against standard samples of ^{152}Eu, ^{54}Mn, ^{57}Co, ^{65}Zn, ^{88}Y, ^{133}Ba, ^{137}Cs and ^{139}Ce. Coincidence summing corrections /5/ were applied at the closer distances. Half lives and transition probabilities were taken from published compilations /6/.

The gamma background at the site was not satisfactory even inside a 10 cm thick lead shield. Presumably due to the LAMPF stack effluent there was an extremely high background caused by the 511 keV annihilation radiation. There was in addition background from isotopes that were to be identified in the experiment (^{59}Fe, ^{58}Co, ^{56}Co, ^{54}Mn). The background problem seriously limited counting at lower levels, i.e. activities could not be obtained beyond certain depths in the shield.

III. EXPERIMENTAL RESULTS AND DATA REDUCTION

All foil activities were corrected for self absorption in the foils, for decay during irradiation utilizing the recorded ^{3}He-detector counts, and for decay during counting. They are for the time at the end of bombardment. The final reaction rates are normalized to the number of primary protons interacting in the target and the number of foil nuclei.

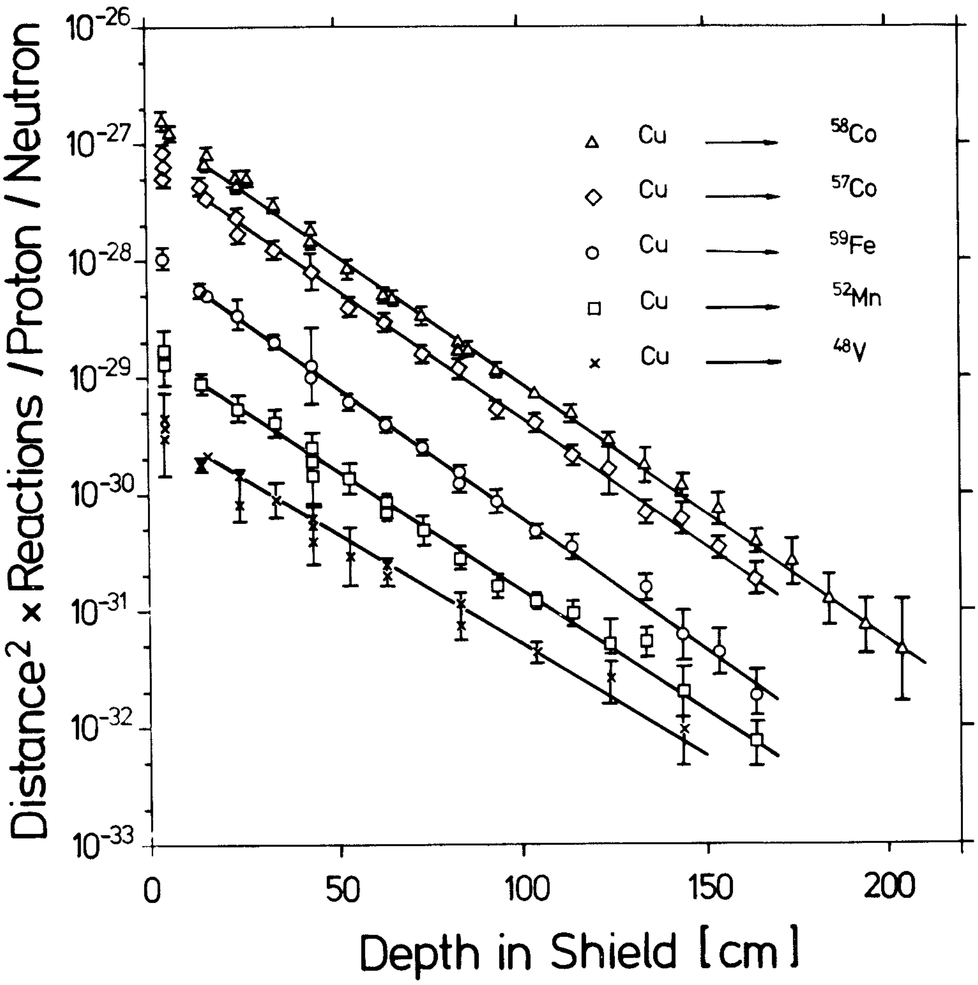

Fig. 3: Depth dependence of the reaction rates for some reactions on copper of natural isotopic composition. To eliminate solid angle dependence the reaction rates have been multiplied by the distance to the target center squared

These reaction rates have been multiplied by the distance to the target squared and have been plotted versus depth in the shield. Results for some spallation reactions on copper are shown in Fig. 3 and 4. Results for all other reactions investigated are given in Appendix A.

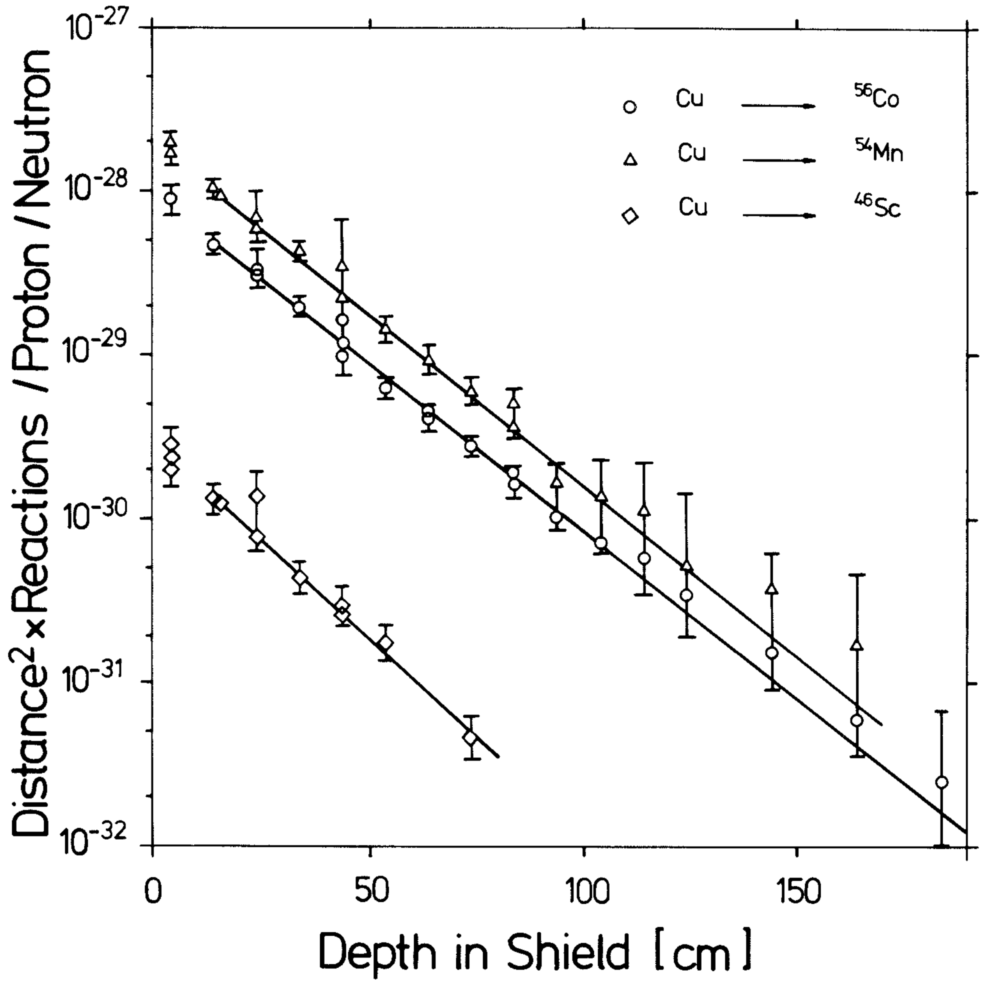

Fig. 4: Depth dependence of the reaction rates for some reactions on copper of natural isotopic compositions. To eliminate solid angle dependence the reaction rates have been multiplied by the distance to the target center squared

The ^{3}He-monitor normalization turned out to be very reliable to within less than 8%. This follows by comparing copper reaction products from different runs for positions farther inside the shield. At positions closer to the target the consistency is not very good. This might be due to fluctuations of the beam position on target which results in a somewhat more pronounced unisotropy for low-energy neutrons than for the deep penetrating high-energy neutrons.

IV. HIGH ENERGY TRANSPORT CALCULATION PROCEDURE

Combined Monte Carlo and deterministic transport calculations were performed for the experimental arrangement of Fig. 2 to calculate the reaction rates for the measured reactions on copper. Two important simplifications can be done due to the fact that nearly all reactions used in the experiments have threshold energies above 15 MeV.

1. It is not necessary to follow neutrons in energy below 15 MeV, i.e. it is adequate to use only the Monte Carlo code HET/KFA-1 with a cut-off energy at 15 MeV and neglect subsequent low-energy transport calculations.
2. It is allowed to simplify the complex moderator-reflector system surrounding the target (see Fig. 2) and simply describe it as a homogeneous beryllium cylinder, because in the shielding context the entire system is of interest only for removing high energy particles. The low energy particles stemming from moderations will not be measured by the threshold detectors and can, therefore, be neglected in the shielding calculations.

This simplifies our shielding calculation as compared to target calculations.

The particle histories were calculated with HET/KFA-1 down to the lower energy limit of 15 MeV. The histories were started by incoming protons of 800 MeV hitting the top surface of the cylindrical tungsten target. The particle fluxes inside the shield were determined in two different ways:

1. Straight forward Monte Carlo with HETC and SIMPEL analysis. The code SIMPEL of the system /2/ calculated neutron fluxes and proton fluxes at different depths inside the shield using tracklength estimators.
2. HETC-ANISN surface coupling procedure via SIMPEL.

Close to the inner surface of the bulk shield a spherical segment was defined serving as a coupling surface between SIMPEL and ANISN. Here SIMPEL calculated a neutron surface source, which was handed over to the one-dimensional transport code ANISN. Starting with this source, ANISN calculated the neutron fluxes inside the shield in spherical geometry. The coupling procedure is described in Appendix B. The transport cross sections used for the calculations were taken from the LANL library /7/. The group structure boundaries of this library in the energy range from 800 MeV to 15 MeV are given in Table II.

Table II: 41-Group Structure Energy Boundaries above 15 MeV of Ref. /7/

Group No.	Upper Bound (eV)
1	8.00×10^8
2	7.00×10^8
3	6.00×10^8
4	5.00×10^8
5	4.00×10^8
6	3.00×10^8
7	2.00×10^8
8	1.00×10^8
9	5.00×10^7
10	2.50×10^7
11	2.00×10^7
12	1.70×10^7
lower bound	1.50×10^7

Both HET/KFA-1 and ANISN calculated fluxes were folded with corresponding reaction cross sections to obtain reaction rates. Two sets of cross sections were generated using the RUDSTAM formulas /8/ and the code ALICE /9/, respectively.

Geometry

The geometrical layout for the HETC calculations was described using concentrical cylinders (see Fig. 5) with the following zones and materials:

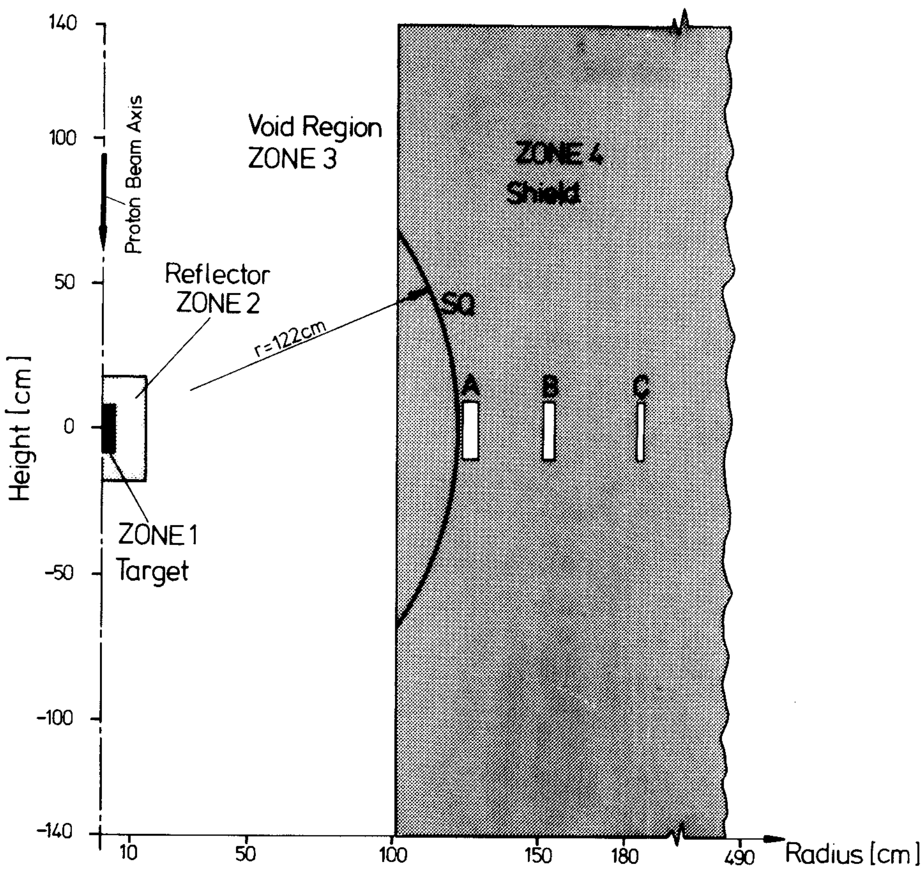

Fig. 5: Geometry setup for radiation transport calculations

Zone 1 was the tungsten target, zone 2 the beryllium reflector - the simplifying assumption for the moderator-reflector system. The radius of this reflector was set to the actual thickness in the experimental arrangement for flight path 5 (FP5) from the target center to the center of the inner surface of the stringer. Zone 3 is a void region and zone 4 is the shield which consists of a mixture of iron and concrete. Dimensions and material compositions of all four zones are given in Table III.

Table III: Materials and Geometry for the HET/KFA-1 Calculation

Description	Zone No.	Outer radius (cm)	cylinder bottom (cm)	top (cm)	Material	Density (atoms x $10^{24}/cm^3$)
W-Target	1	2.225	- 7	8	^{182}W	$1.64x10^{-2}$
					^{183}W	$8.83x10^{-3}$
					^{184}W	$1.96x10^{-2}$
					^{188}W	$1.83x10^{-2}$
Be-Reflector	2	15	-17	18	^{9}Be	$1.24x10^{-1}$
Cavity	3	101.5	-140	140	void	
Shield	4	490	-140	140	^{1}H	$1.47x10^{-4}$
					^{16}O	$1.5x10^{-3}$
					^{27}Al	$4.84x10^{-6}$
					^{28}Si	$1.93x10^{-4}$
					^{40}Ca	$3.73x10^{-4}$
					^{54}Fe	$4.63x10^{-3}$
					^{56}Fe	$7.11x10^{-2}$
					^{57}Fe	$1.54x10^{-3}$

For the flux estimation from HETC histories SIMPEL used track length estimators which were rings of 20 cm height each and thicknesses of about 3 cm. These volume detectors are denoted A, B, C in Fig. 5. The advantage of such ring shaped detectors is the strongly enhanced statistics due to the azimuthal symmetry as compared to small detector boxes.

The coupling surface of the neutron surface source used by ANISN (denoted SQ in Fig. 5) was a spherical segment with radius 122 cm. This segment was placed entirely into the bulk shield. This geometry is not azimuthal symmetric. For the ANISN transport calculations beyond the coupling surface the bulk shield was assumed to be composed of iron only with nuclide density 8.44×10^{22} atoms x cm^{-3}. This is supposed to be the better approximation to the surrounding environment of the monitor foils inside the stringer than the iron/concrete mixture of the bulk shield.

V. THEORETICAL RESULTS

HETC and the HETC-ANISN coupling procedure calculate particle fluxes for energies between 800 MeV and 15 MeV at different depths inside the shield. The proton flux is negligable as compared to the neutron flux as Table IV shows. Therefore, protons have been neglected in all calculations following. Looking at the depth dependence in Table IV, a comparison of the HETC-ANISN coupling and HETC results shows, that the high energy flux as calculated by HETC is not decreasing as fast as predicted by the HETC-ANISN coupling while going further into the shield. The reason for this behaviour could be that for the HETC calculation a mixture of iron and concrete with an iron number density of 7.7×10^{22} atoms x cm^{-3} was assumed, while for the HETC-ANISN coupling calculation pure iron with a number density of 8.44×10^{22} atoms x cm^{-3} was used to account for the true material composition inside the stringer.

Table IV: Total Flux per cm^2 and per incident proton

Depth in Shield	Position in Fig. 5	HETC protons	HETC neutron	HETC-ANISN-coupling neutrons
23 cm	A	6.38×10^{-9}	1.48×10^{-6}	1.85×10^{-6}
103 cm	B	0	1.70×10^{-8}	8.60×10^{-9}
203 cm	C	0	0	1.90×10^{-11}

Flux Spectra

Fig. 6 shows a comparison of the flux spectra calculated by HETC at two different depths inside the shield. At 23 cm the spectrum is harder than at 103 cm depth. The reason could be that the mixture of iron and concrete acts as a moderator. But it should be mentioned that at 103 cm depth the fractional standard deviation values (FSD) for all energy groups of the spectrum are in the range of about 50 percent. To compare the predictions of the spectral behaviour of both procedures the spectrum calculated by the HETC-ANISN coupling and the HETC spectrum are plotted in Fig. 7 at 23 cm depth. We have chosen this position because it is very close to the coupling surface SQ in Fig. 5 and good statistics can be obtained with HETC itself. As expected, good agreement between both spectra is obtained.

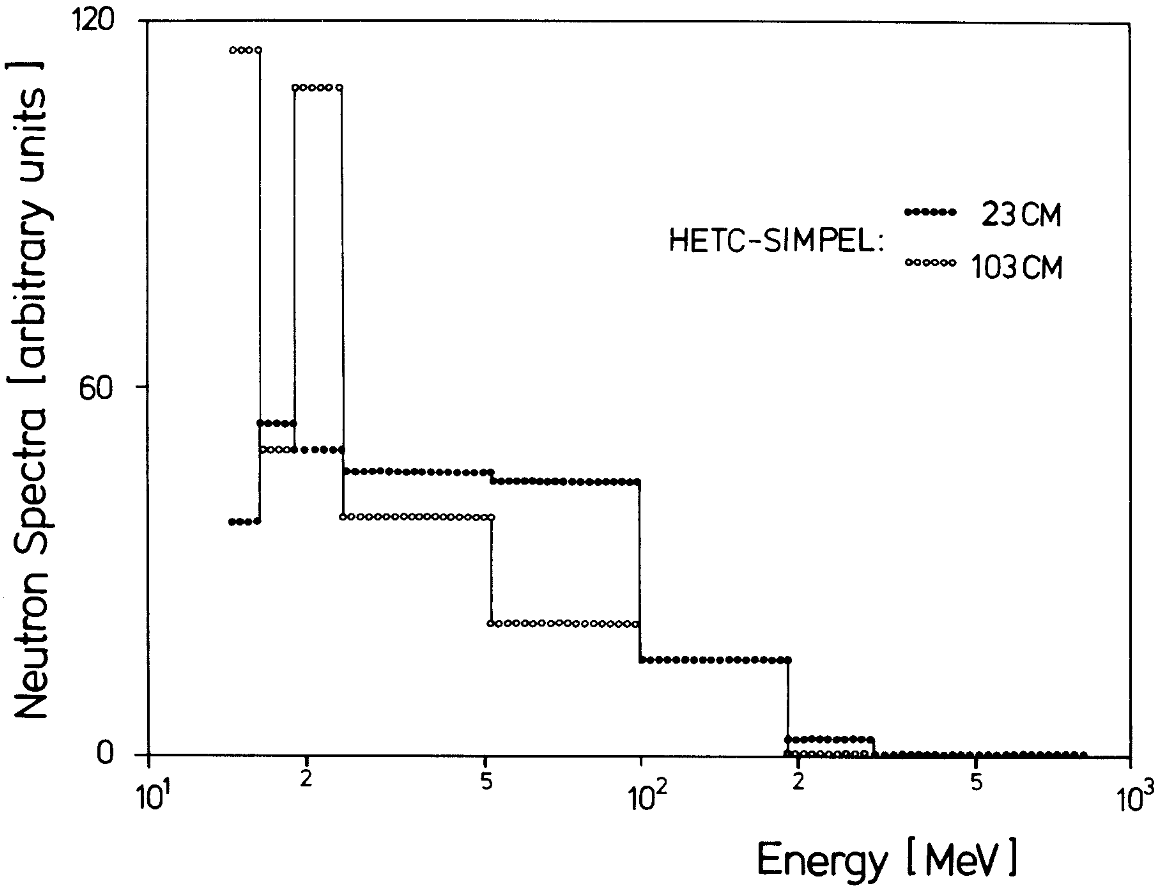

Fig. 6: HETC-SIMPEL straight forward calculations

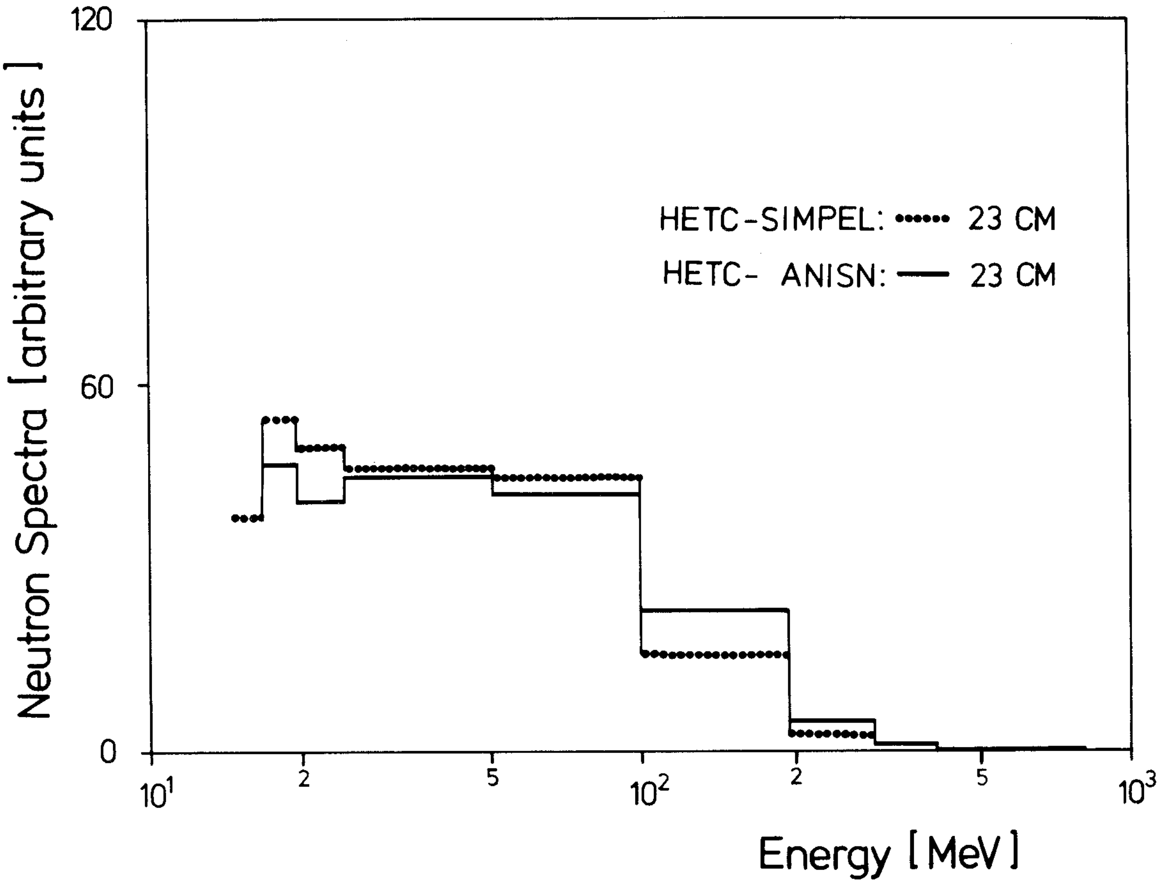

Fig. 7: Comparison of HETC-ANISN and HETC calculations

Fig. 8 gives the spectra calculated by the HETC-ANISN coupling at three different depths. In contrast to the spectrum behaviour calculated by HETC (Fig. 6), the HETC-ANISN coupling spectrum is harder at 103 cm than at 23 cm depth. Furthermore, Fig. 8 shows that the spectra at 103 cm depth and in 203 cm are nearly identical. Therefore, it can be stated that the HETC-ANISN coupling spectra reach equilibrium very fast.

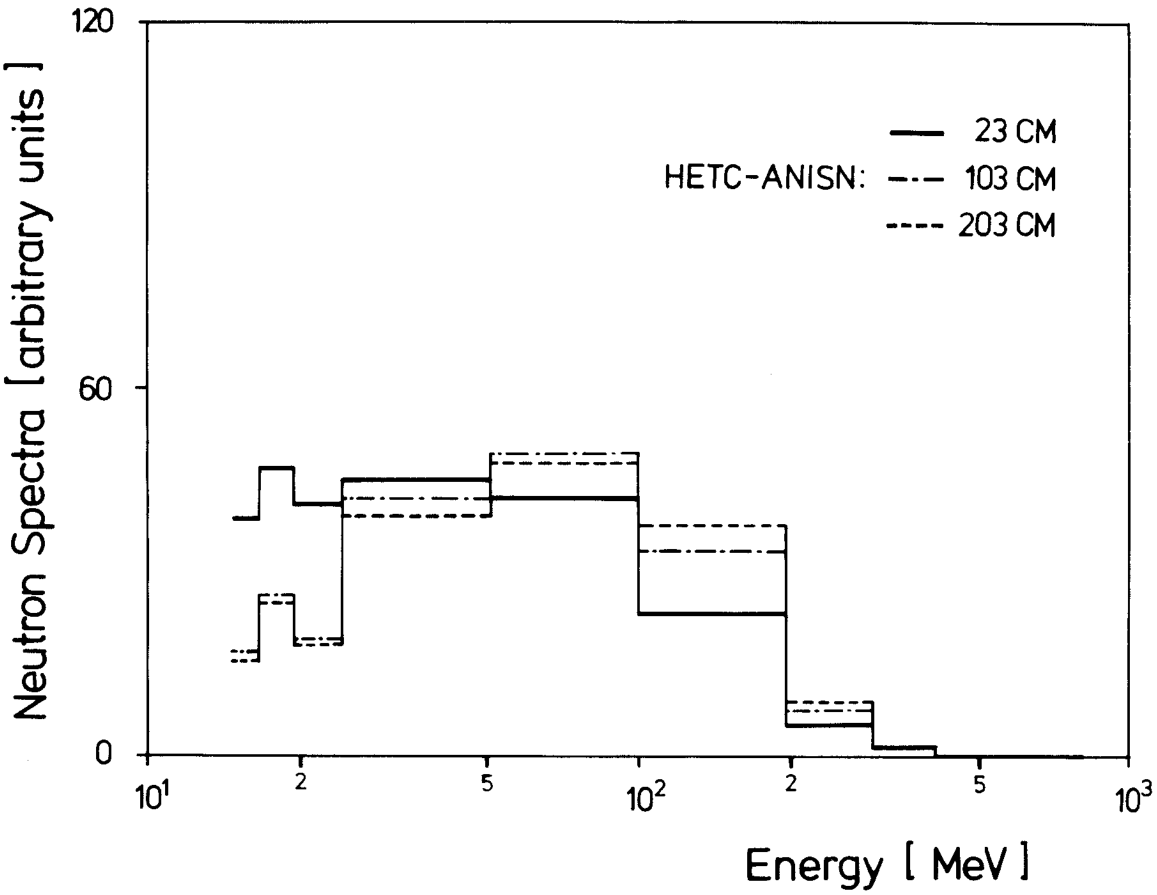

Fig. 8: HETC-ANISN calculations

Reaction Rates

Calculated results that can be compared with the experiments directly are the threshold reaction rates. They were calculated by folding the group dependent neutron fluxes with reaction cross sections. Such reaction rates were generated for two positions at 23 cm and 103 cm. In Table V the calculated and measured rates for the reactions on foils of natural copper are shown. Agreement within a factor of two between measured and calculated reaction rates is found for the Rudstam cross sections. It should be mentioned, however, that both the measured reaction rates and the calculated fluxes contain uncertainties of up to 50 percent (see spectrum results in Figs. 6-8 and tables in Appendix C). Much larger differences between measurement and calculation up to more than a factor of 10 are found if reaction cross sections generated by the code ALICE are used to calculate the reaction rates.

Table V: Comparison of calculated and measured reaction rates per foil nucleon and per incident proton

Cu-nat	Experiment Run 1	Rudstam HETC-ANISN coupling	Rudstam HETC	ALICE HETC-ANISN coupling
		d = 23 cm		
Fe-59	2.1×10^{-33}	4.7×10^{-33}	3.5×10^{-33}	3.7×10^{-33}
Co-58	2.8×10^{-32}	4.5×10^{-32}	3.2×10^{-32}	9.3×10^{-32}
Co-57	1.4×10^{-32}	1.2×10^{-32}	0.8×10^{-32}	5.0×10^{-32}
Co-56	2.0×10^{-33}	2.4×10^{-33}	1.5×10^{-33}	16.0×10^{-33}
Mn-52	3.5×10^{-34}	6.3×10^{-34}	3.6×10^{-34}	60.0×10^{-34}
Mn-54	3.9×10^{-33}	5.3×10^{-33}	3.3×10^{-33}	14.0×10^{-33}
V-48	0.5×10^{-34}	1.0×10^{-34}	1.1×10^{-34}	20.0×10^{-34}
		d = 103 cm		
Fe-59	1.1×10^{-35}	2.7×10^{-35}	2.8×10^{-35}	1.8×10^{-35}
Co-58	1.8×10^{-34}	2.6×10^{-34}	2.5×10^{-34}	4.6×10^{-34}
Co-57	9.5×10^{-35}	7.5×10^{-35}	6.9×10^{-35}	27.0×10^{-35}
Co-56	1.7×10^{-35}	1.5×10^{-35}	1.3×10^{-35}	9.4×10^{-35}
Mn-52	2.8×10^{-36}	4.1×10^{-36}	3.2×10^{-36}	38.0×10^{-36}
Mn-54	3.2×10^{-35}	3.3×10^{-35}	2.8×10^{-35}	8.7×10^{-35}
V-48	1.0×10^{-36}	1.4×10^{-36}	0.9×10^{-36}	13.0×10^{-36}

VI. DISCUSSION

In comparing experiment and calculations two different major sources of uncertainties have to be considered: the reaction cross sections for the production of residual nuclei in the monitor foils by neutrons, and the influence of other particles, mainly protons.

As has been mentioned in section IV, protons have been neglected inside the shield. But this is a very good approximation, because the calculated proton flux is much lower than for neutrons. Based on the assumption of equal cross sections for neutrons and protons, about 1% higher reaction rates would be calculated if protons would be considered in equal proportions everywhere (Table IV). Due to the relatively low energies (<100 MeV) and the high energy loss, secondary neutron production by protons in the shield can be neglected. The total influence of protons, therefore, would be to increase the reaction rates by an amount totally negligable against all other sources of uncertainties which have been discussed.

The most serious source of uncertainty are the neutron production cross sections for the respective monitor reactions. In most evaluations it is simplistically assumed that at high energies (above 20 MeV) spallation cross sections for protons and neutrons are identical. The common description of this process as an intranuclear cascade and a subsequent evaporation process is in favour of this idea of equal response to both nucleons. Therefore, following Routti's approach cross sections for proton induced reactions which are much easier to obtain experimentally than neutron cross sections were compiled and treated like neutron cross sections to calculate the reaction rates at different positions in the shield. Sources of cross sections were the Rudstam /8/ formulas, which are semiempirical parameterizations of experimental results up to 1964, the modifications by Silberberg and Tsao /10/, more recent experiments on copper targets reported by Orth /11/, Grütter /12/, Williams /13/ and Greenwood /14/ and, finally, preequilibrium calculations with ALICE /9/.

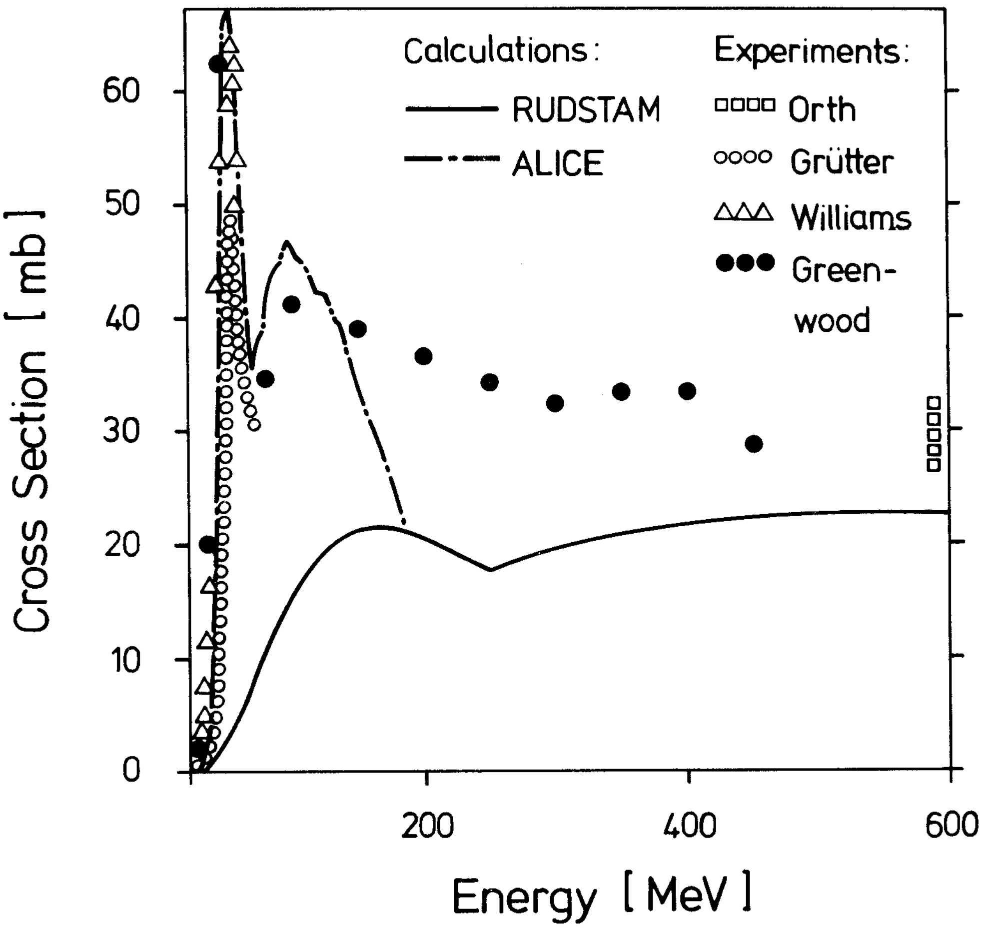

Fig. 9: Experimental cross sections /11-14/ and model calculations /8,9/ for the production of ^{57}Co from copper

For three examples part of the compilations are shown in Figs. 9 to 11. For all other reactions listed in Table V the present compilations are given in Appendix D. The Silberberg/Tsao cross sections have not been included in the plots because their general shape follows Rudstam's curves with up to 50% deviation to both sides. In Fig. 9 the agreement between experiments and ALICE calculations for the production of ^{57}Co from copper is reasonable in the region close to the threshold energy. At higher energies they disagree strongly with ALICE predicting a steep decrease. Rudstam's curve is systematically too low, Silberberg/ Tsao's prediction would hit the last point of Greenwood's experiment. The resulting large difference between the reaction rates calculated from both Rudstam's and ALICE's cross sections is found in Table V for ^{57}Co. The experimental reaction rate in Table V should be closer to the reaction rate obtained by folding the calculated neutron flux with ALICE's cross sections. But these cross sections seem to be the upper limits as compared to the more recent experimental cross sections.

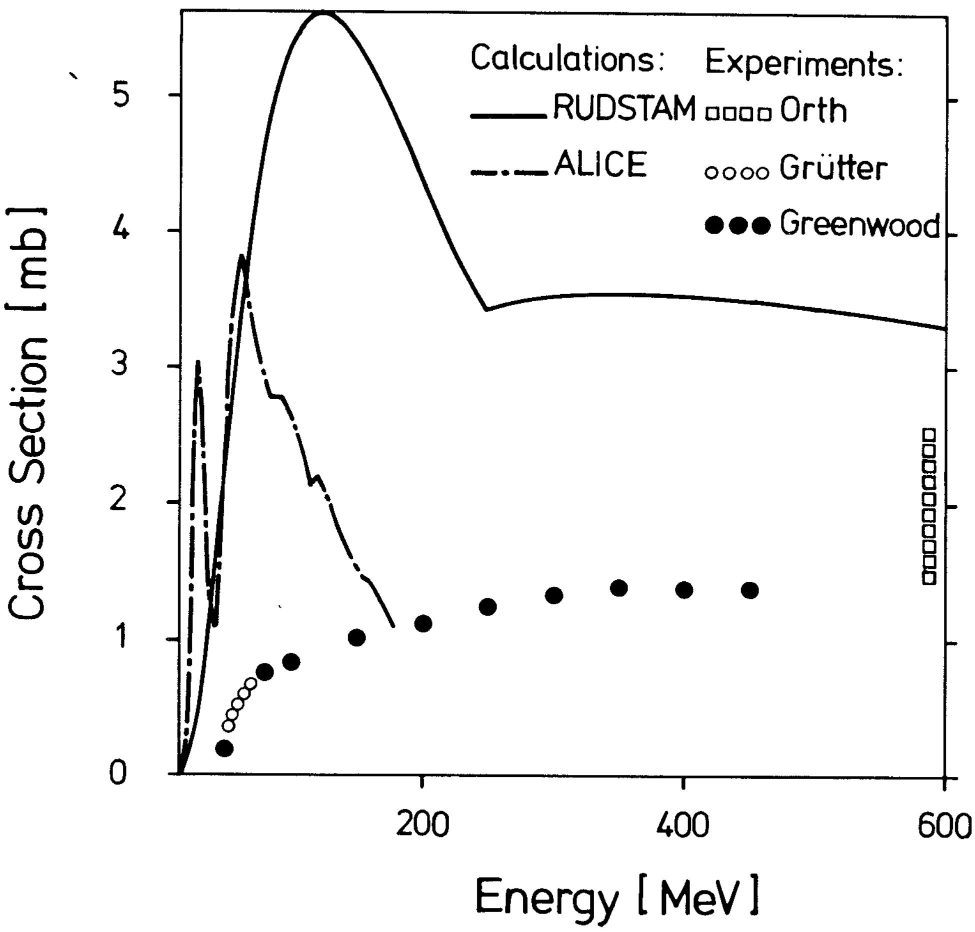

Fig. 10: Experimental cross sections /11-14/ and model calculations /8,9/ for the production of ^{59}Fe from copper

A totally different situation is shown in Fig. 10 for ^{59}Fe from copper where both ALICE's and Rudstam's cross sections are strongly overestimating the results of Grütter and Greenwood. The corresponding reaction rates are indeed overestimating the experimental rate by factors of two to three.

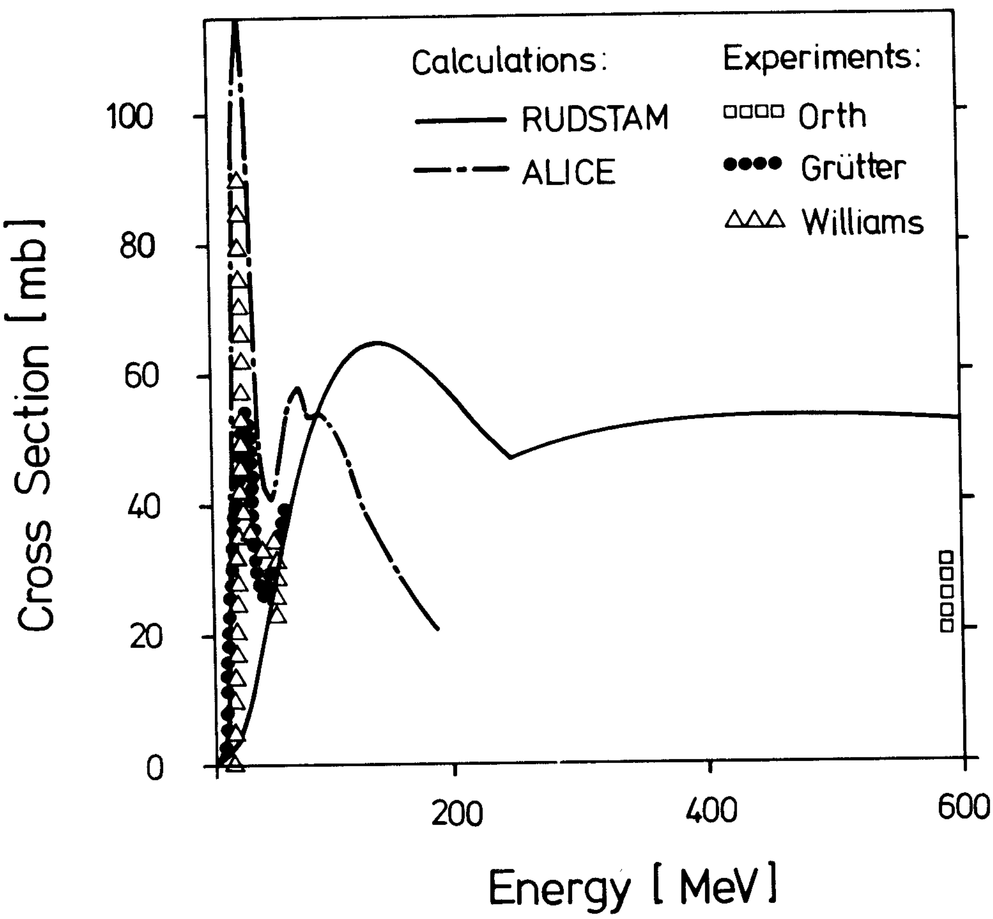

Fig. 11: Experimental cross sections /11-14/ and model calculations /8,9/ for the production of ^{58}Co from copper

For the production of ^{58}Co from copper the trend of disagreement between experimental and calculated reaction rates in Table V cannot be explained from cross sections alone as Fig. 11 shows. Based on the recent experiments of Grüttner and Williams the experimental reaction rate from ^{58}Co in

Table V should be between ALICE's and Rudstam's prediction. This is definitely not the case. In this case it would be a strong argument to assume that the neutron cross section at the low threshold energy would certainly be different for the proton cross sections.

The most striking feature in this discussion is that we can only argue within factors of two or three or more from cross sections alone. The total disagreement between ALICE's and Rudstam's (or Silberberg/Tsao's) cross sections and experimental values makes any evaluation effort obsolete. ALICE seems to follow the general shape of the experimental results better than the Rudstam formulas, but still showing large discrepancies. Under this aspect there is a strong need for cross section measurements especially above 70 MeV to produce a reliable data base. Not until cross sections have been obtained with small enough uncertainties (of at least better than a factor of 2) and sufficiently narrow energy spacings at the threshold energies, more accurate comparisons between experiment and calculations at high neutron energies cannot be expected.

VII. CONCLUSION

The deep penetration experiment at the WNR helped to generate an experimental data base for a well defined spallation physics environment to be compared with predictions of the HETC/KFA-1, and ANISN codes. The experiment's position perpendicular to the beam axis excluded primary protons and most of the high-energy neutrons beyond the evaporation neutron energies. This made especially the HETC calculations more elaborate, because most of the histories are in forward direction or are confined within the target/reflector volume. To get enough statistics perpendicular to the beam axis 122 cm away from the target calls certainly for more CPU time, but without making all simplifying assumptions and taking full advantage of the approximate symmetry of the WNR target, CPU time would be unreasonably high.

The direct comparison between experiment and calculation was based on the measured reaction rates, any unfolding of the experimental data would have introduced additional sources of uncertainty beyond cross sections. The agreement is not too satisfactory, but as the compilation of reaction cross sections for natural copper targets shows, cross sections alone are the largest source of uncertainty, larger than Monte Carlo statistics, coupling between codes or proton contributions. The results presented show that experiment and both HETC and HETC-ANISN coupling calculations do compare to some extent, but the overall uncertainties introduced by the cross section for the specific reaction excludes conclusions as to how to improve the calculational model.

Basically one has to conclude that cross sections for the neutron detection reactions studied have to be measured first with reasonable accuracy to provide a reliable base for comparing experiment and calculation. The lack of experimental cross sections above 20 MeV is certainly due to the fact that accelerators with variable particle energies between 1 GeV and 20 MeV are not available. The proposed COSY synchrotron that will produce protons between 40 MeV and 2.5 GeV would be the ideal facility to measure the required cross sections.

Acknowledgements

The authors would like to thank Richard Woods of LANL Physics Division and all other members of his group for their kind hospitality and continuous support.

Special thanks to the operators and other personnel associated with the WNR facility for their assistance with the irradiations.

VIII. REFERENCES

/1/ R. Woods
Proceedings of the 5th Meeting of International Collaboration on Advanced Neutron Sources (ICANS-V)
Jülich, June 22-26, 1981, Jül-Conf-45, October 1981

/2/ P. Cloth, D. Filges, G. Sterzenbach, T.W. Armstrong, B.L. Colborn
The KFA-Version of the High-Energy Transport Code HETC and the generalized Evaluation Code SIMPEL
Report Jül-Spez-196, March 1983

/3/ W.W. Engle
Report ORNL-1693, 1973

/4/ J.T. Routti, J. Tapio
High-Energy Neutron Spectroscopy with Activation Detectors
Report UCRL-18514, 1969

/5/ W. Amian, N. Paul
Internal KFA Report, SNQ A1022.1-, May 1985

/6/ G. Erdtmann, W. Soyka
The Gamma Rays of the Radionuclides
Verlag Chemie, Weinheim and New York, 1979

/7/ W.B. Wilson
Report LA-7159-T, 1978

/8/ G. Rudstam
Zeitschrift für Naturforschung 21, 1027, 1966
see also: J.T. Routti, J.V. Sandberg
Computer Physics Communications
23, 411, 1981

/9/ M. Blann
Phys. Rev. Lett. 27, 337 1971
and UCID 19614, 1982

/10/ R. Silberberg, C.H. Tsao
The Astrophysical Journal Supplement Series No. 220(I), 25, 315 & 335, 1973

/11/ C.J. Orth et al.
Journal of Inorganic Nuclear Chemistry 38, 13, 1976

/12/ A. Grütter
Nucl.Phys. A 383, 98, 1982

/13/ I.R. Williams, C.B. Fulmer
Phys. Rev. 162, 1055, 1967

/14/ L.R. Greenwood, R.K. Smither
Report DOE-ER-0046/14, 1983

/15/ R. Michel et al.
Nuclear Physics A441, 617-639, 1985

/16/ R. Michel, R. Stück
Proceedings of the 14th Lunar and Planetary Science Conference, Part 2
Journal of Geophysical Research, Vol. 89, Supplement B673-B684, 1984

/17/ Bronstein, Semendjajew
Taschenbuch der Mathematik, Harri Deutsch Verlag, Zürich und Frankfurt/M., 1965

IX. APPENDIX A

Experimental Reaction Rates

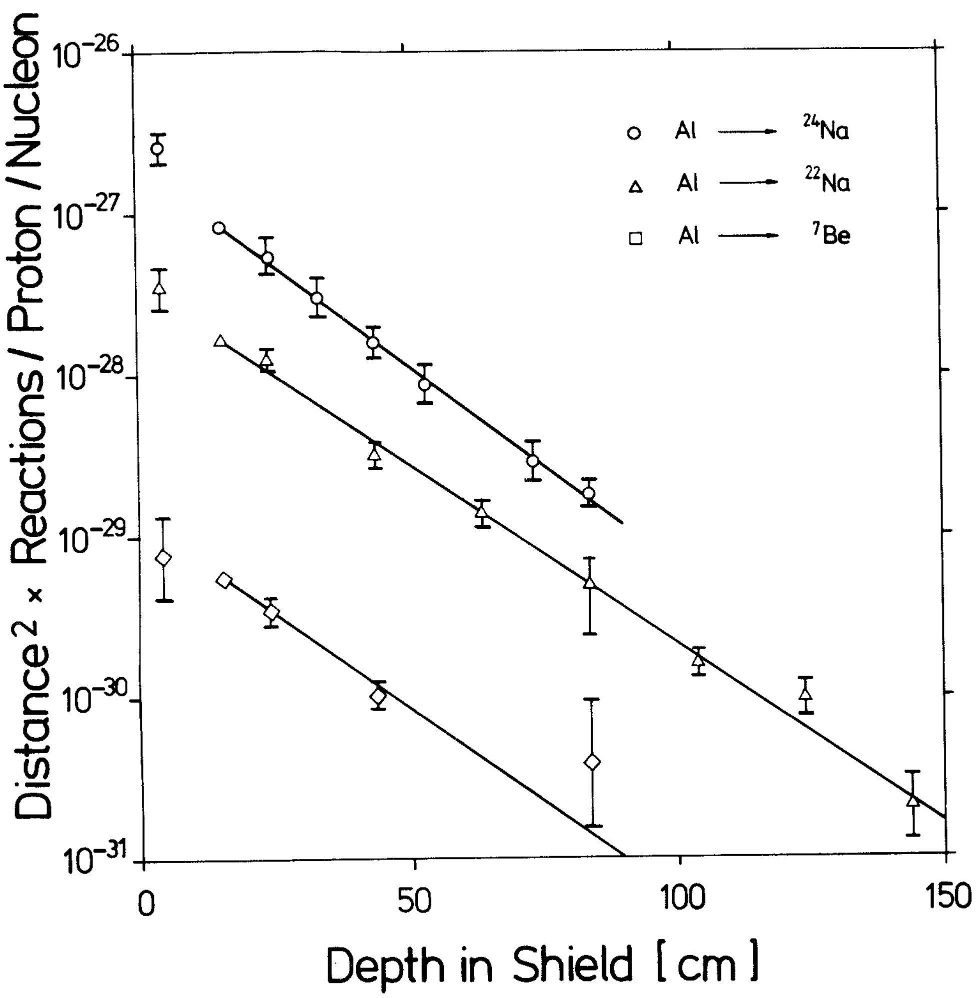

Fig. A.1 Depth dependence of the reaction rates for some reactions on aluminum. To eliminate solid angle dependence the reaction rates have been multiplied by the distance to the target center squared

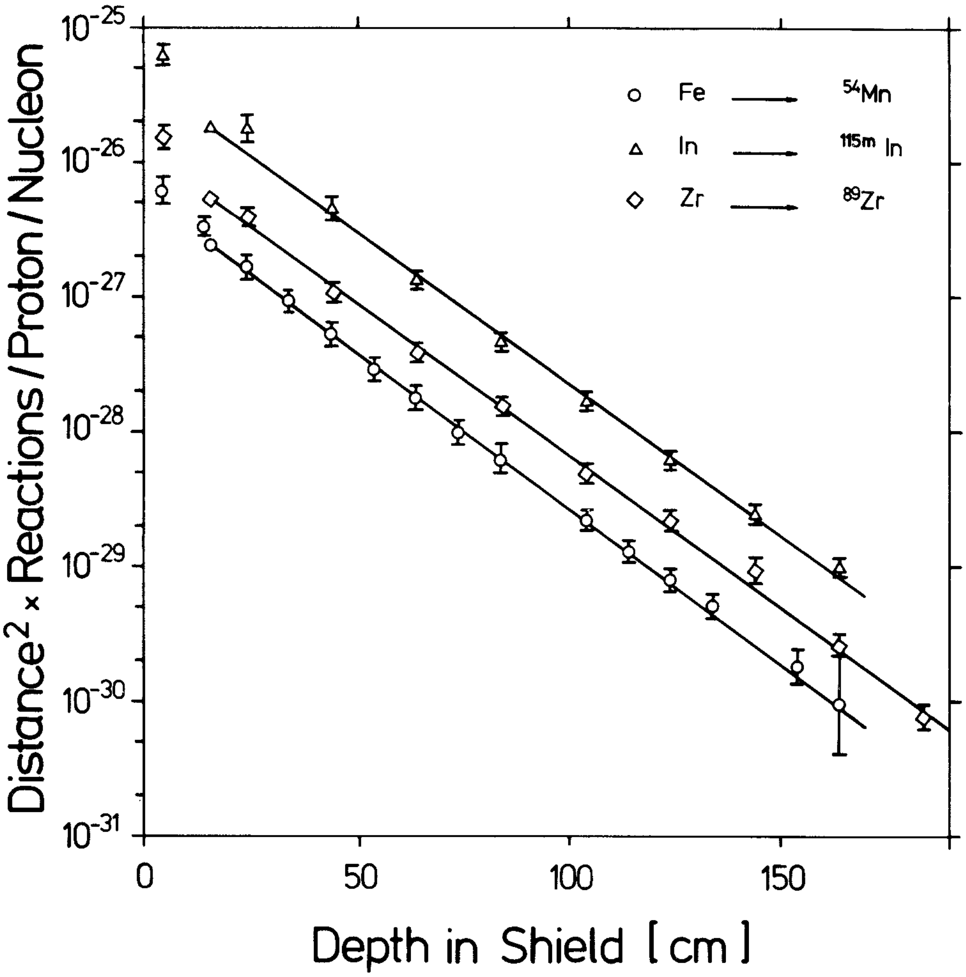

Fig. A.2 Depth dependence of the reaction rates for some reactions on iron, indium and zirconium of natural isotopic composition. To eliminate solid angle dependence the reaction rates have been multiplied by the distance to the target center squared

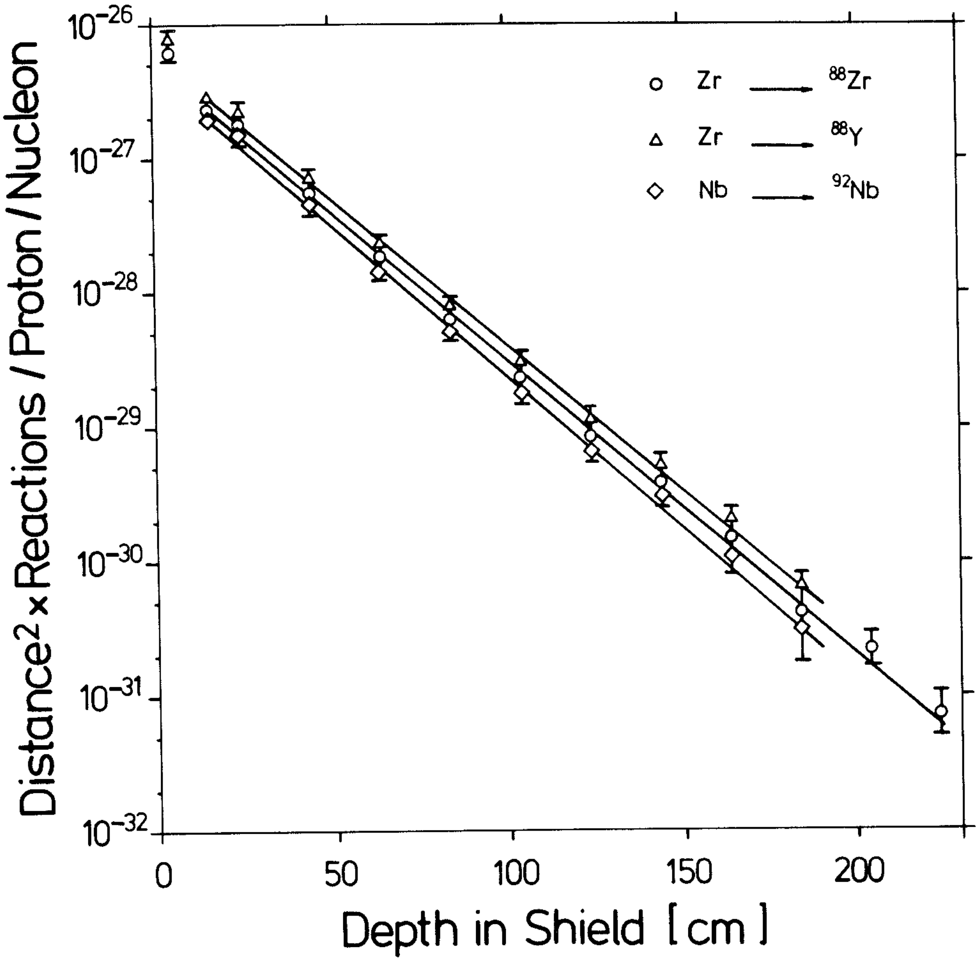

Fig. A.3 Depth dependence of the reaction rates for some reactions on zirconium and niobium of natural isotopic composition. To eliminate solid angle dependence the reaction rates have been multiplied by the distance to the target center squared

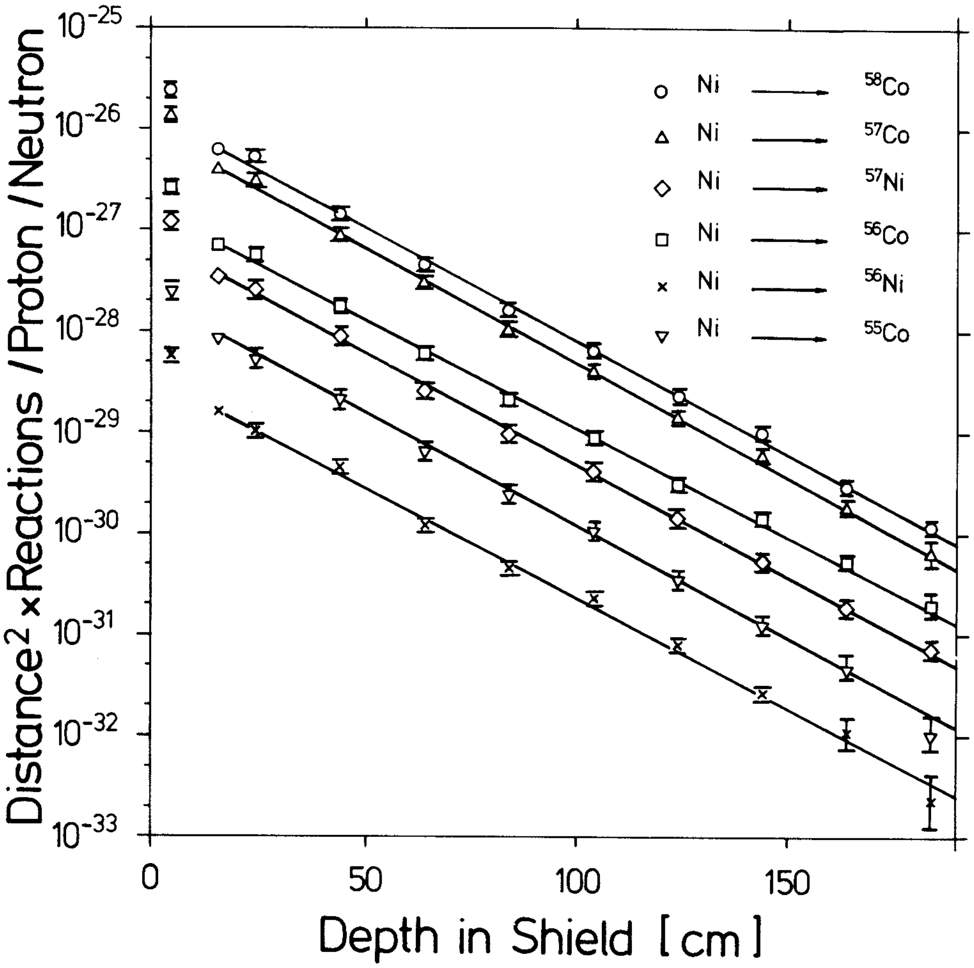

Fig. A.4 Depth dependence of the reaction rates for some reactions on nickel of natural isotopic composition. To eliminate solid angle dependence the reaction rates have been multiplied by the distance to the target center squared

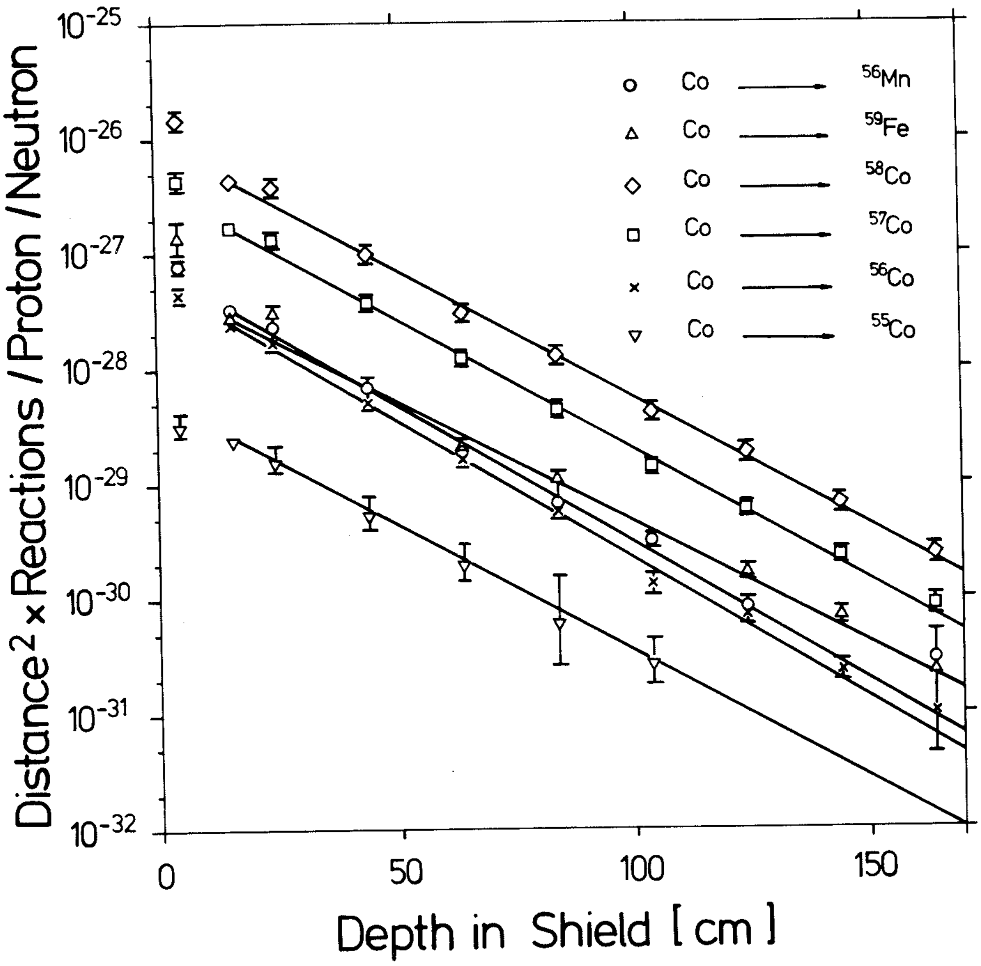

Fig. A.5 Depth dependence of the reaction rates for some reactions on cobalt. To eliminate solid angle dependence the reaction rates have been multiplied by the distance to the target center squared

X. Appendix B

HETC-ANISN Surface Flux Coupling Procedure

1. Calculation of the surface flux with HETC-SIMPEL-System

We decided that the surface flux generated by SIMPEL should be handed over to ANISN as an expansion of Legendre-polynomials. The advantage of this method - compared to a binning procedure - is that for different S_N-sets in ANISN always the same set of polynomial coefficients can be used. Now we show how to get the Legendre coefficients from the Monte Carlo events:

An event i in direction x_i with the statistical weight g_i adds up to the neutron flux $\phi(x)$ as

$$\phi_i(x) = g_i \; \delta(x-x_i) \tag{1}$$

The flux $\phi(x)$ then is

$$\phi(x) = \sum_i \phi_i(x) = \sum_i g_i \delta(x-x_i) \tag{2}$$

Because we want to generate Legendre expansion, we make the statement

$$\delta(x-x_i) = \sum_{k=0}^{N} d_{i,k} \cdot P_k(x) \cdot b_k \tag{3}$$

with

$$b_k = \frac{2k+1}{2}$$

Normally in the sum N should go to infinity. We restrict ourselves to N, say 50 in hoping that values $d_{i,k}$ for k>N do not influence the result significantly.

Introducing eq. (3) into eq. (2) leads to

$$\phi(x) = \sum_i g_i \sum_{k=0}^{N} b_k \cdot d_{i,k} \cdot P_k(x) = \sum_{k=0}^{N} (\sum_i g_i \, d_{i,k}) \cdot P_k(x) \cdot b_k \qquad (4)$$

We are interested in coefficients A_k, which are defined by

$$\phi(x) = \sum_{k=0}^{N} b_k \cdot A_k \cdot P_k(x) \qquad (5)$$

and which can be got by comparison of eq. (5) with eq. (4):

$$A_k = \sum_i g_i \cdot d_{i,k} \qquad (6)$$

This set of A_k, which is to calculate for each energy group, is handed over from SIMPEL to the transport code ANISN.

The statistical weights g_i in eq. (6) SIMPEL gets from the code HETC, the coefficients $d_{i,k}$ are calculated in SIMPEL as follows:

Starting from eq. (3) both sides of this equation are multiplied with $P_n(x)$ and integrated over the entire region of definition from −1 to +1,

$$\int_{-1}^{+1} P_n(x) \, \delta(x-x_i) dx = \int_{-1}^{+1} P_n(x) \sum_{k=0}^{N} d^i{}_k \cdot P_k(x) dx \cdot b_k \qquad (7)$$

The left hand side of eq. (7) leads to $P_n(x_i)$, the right hand side reduces the sum to one element only because of the orthogonality of the Legendre functions. So we get

$$P_n(x_i) = d_{i,n} \int_{-1}^{+1} \{P_n(x)\}^2 dx \, b_n = d_{i,n} \frac{2}{2n+1} b_n \qquad (8)$$

So the wanted values $d_{i,k}$ of eq. (6) are got from eq. (8) as

$$d_{i,k} = P_k(x_i) \tag{9}$$

To calculate the values $d_{i,k}$ for all k without tabulating the functions $P_k(x)$, we use the recurrance formula (ref. 17) for Legendre functions:

$$P_k(x) = \frac{2k-1}{k} \cdot x \cdot P_{k-1}(x) - \frac{k-1}{k} P_{k-2}(x) \tag{10}$$

It can be seen that knowing $P_0(x_i)$ and $P_1(x_i)$ all values $P_k(x_i)$ for k>1 and then all $d_{i,k}$ can be calculated in a recursive manner. Eq. (6) then gives the desired values A_k.

2. Calculation of the surface source in ANISN

The surface source in ANISN for the angular interval from angle ψ_{n-1} to ψ_n, i.e. from $x_{n-1} = \cos \psi_{n-1}$ to $x_n = \cos \psi_n$ is

$$S_n = \int_{x_{n-1}}^{x_n} \phi(x)dx \tag{11}$$

In the previous section we defined (see eq. (5))

$$\phi(x) = \sum_{k=0}^{N} b_k \cdot A_k \cdot P_k(x) \tag{12}$$

with $b_k = (2k+1)/2$ and A_k given from SIMPEL calculation. So the desired source S_n reads

$$S_n = \sum_{k=0}^{N} b_k \cdot A_k \int_{x_{n-1}}^{x_n} P_k(x)dx \tag{13}$$

We define

$$I_{k,n} = \int_{x_{n-1}}^{x_n} P_k(x)dx \qquad (14)$$

and get

$$S_n = \sum_{k=0}^{N} b_k A_k I_{k,n} \qquad (15)$$

With statement

$$P_k(x) = \sum_{l=0}^{k} a_{k,l} \cdot x^l \qquad (16)$$

we can perform the integration of eq. (14) as

$$I_{k,n} = \sum_{l=0}^{k} \frac{1}{l+1} a_{k,l} \cdot \{(x_n)^{l+1} - (x_{n-1})^{l+1}\} \qquad (17)$$

It remains to determine the coefficients $a_{k,l}$.
This is done as follows: The statement (see eq. (16)) we write as

$$P_{k+1}(x) = \sum_{l=0}^{k+1} a_{k+1,l} \cdot x^l \qquad (18)$$

On the other hand we use the recurrance formula (ref. 17) for k+1 as

$$P_{k+1}(x) = \frac{2k+1}{k+1} \cdot x \cdot P_k(x) - \frac{k}{k+1} P_{k-1}(x) \qquad (19)$$

and compare both relations. The result is

$$\sum_{l=0}^{k+1} a_{k+1,l}\cdot x^{l} = \frac{2k+1}{k+1}\sum_{m=0}^{k} a_{k,m}\cdot x^{m+1} - \frac{k}{k+1}\sum_{n=0}^{k-1} a_{k-1,n}\cdot x^{n} \quad (20)$$

We compare the coefficients for an arbitrary exponent i of the variable x and get the desired recurrance formula for the coefficients $a_{k,l}$ as

$$a_{k+1,i} = \frac{2k+1}{k+1} a_{k,i-1} - \frac{k}{k+1} a_{k-1,i} \quad (21)$$

with i from 0 to k+1,

all $a_{-1}=0$,

and $a_{0,0}=1$, because $P_0(x)=1\cdot x^0$,

$a_{1,1}=1$ and $a_{1,0}=0$, because $P_1(x)=1\cdot x^1+0\cdot x^0$.

With calculated $a_{k,l}$ we can calculate $I_{k,n}$ (see eq. (17)) and then the surface source terms S_n by eq. (15).

XI. APPENDIX C

Neutron Spectra and Group Cross Sections used for the Calculations

Table C.1: Neutron spectrum calculated by HETC for depth 23 cm inside the shield

Energy Group (MeV)	Contribution to Total Flux (per cent)	FSD (per cent)
400 - 300	0.1	100
300 - 200	1.2	20
200 - 100	11.0	7
100 - 50	31.0	4
50 - 25	32.0	5
25 - 20	11.0	8
20 - 17	8.7	8
17 - 15	5.0	10

Total neutron flux per cm^{-2} per incident proton = 1.48×10^{-6} (n cm^{-2} per proton)

Table C.2: Neutron spectrum calculated by code HETC for depth 103 cm inside the shield

Energy Group (MeV)	Contribution to Total Flux (per cent)	FSD (per cent)
400 - 300	0	-
300 - 200	0	-
200 - 100	11.0	49
100 - 50	15.0	51
50 - 25	27.0	35
25 - 20	24.0	51
20 - 17	8.0	54
17 - 15	15.0	51

Total flux (per proton) = 1.70×10^{-8}

Table C.3: Neutron spectrum calculated by code HETC/ANISN for depth 23 cm inside the shield

Energy Group (MeV)	Contribution to Total Flux (per cent)
400 - 300	0.4
300 - 200	2.1
200 - 100	16.0
100 - 50	29.0
50 - 25	31.0
25 - 20	9.0
20 - 17	7.5
17 - 15	5.0

Total flux (per proton) = 1.85×10^{-6}

Table C.4: Neutron spectrum calculated by code HETC/ANISN for depth 103 cm inside the shield

Energy Group (MeV)	Contribution to Total Flux (per cent)
400 - 300	0.4
300 - 200	3.0
200 - 100	23.0
100 - 50	34.0
50 - 25	29.0
25 - 20	4.2
20 - 17	4.2
17 - 15	2.2

Total flux (per proton) = 8.60×10^{-9}

Table C.5: Neutron spectrum calculated by code HETC/ANISN for depth 203 cm inside the shield

Energy Group (MeV)	Contribution to Total Flux (per cent)
400 - 300	0.4
300 - 200	3.6
200 - 100	26.0
100 - 50	33.0
50 - 25	27.0
25 - 20	4.0
20 - 17	4.0
17 - 15	2.0

Total flux (per proton) = 1.90×10^{-11}

Table C.6: Group cross sections of the reaction $Cu_{nat}(n,x)^{59}Fe$

Energy (MeV)	Cross section (mbarn) Rudstam	ALICE
800 - 700	3.12	-
700 - 600	3.25	-
600 - 500	3.38	-
500 - 400	3.49	-
400 - 300	3.54	-
300 - 200	3.66	-
200 - 100	5.25	1.57
100 - 50	4.19	3.13
50 - 25	1.22	2.28
25 - 20	0.183	1.28
20 - 17	0.066	0.093
17 - 15	0.028	5.24×10^{-4}

Table C.7: Group cross sections of the reaction $Cu_{nat}(n,x)^{58}Co$

Energy (MeV)	Cross section (mbarn) Rudstam	ALICE
800 - 700	50.4	-
700 - 600	51.8	-
600 - 500	52.9	-
500 - 400	53.26	-
400 - 300	51.95	-
300 - 200	50.13	-
200 - 100	62.08	34.0
100 - 50	37.53	50.6
50 - 25	6.96	97.6
25 - 20	0.553	0.358
20 - 17	0.149	0
17 - 15	0.048	0

Table C.8: Group cross sections of the reaction $Cu_{nat}(n,x)^{57}Co$

Energy (MeV)	Cross section (mbarn) Rudstam	ALICE
800 - 700	22.3	-
700 - 600	22.6	-
600 - 500	22.7	-
500 - 400	22.2	-
400 - 300	20.84	-
300 - 200	18.79	-
200 - 100	20.15	32.8
100 - 50	9.29	46.5
50 - 25	1.11	27.1
25 - 20	0.046	0
20 - 17	0.009	0
17 - 15	0.002	0

Table C.9: Group cross sections of the reaction $Cu_{nat}(n,x)^{56}Co$

Energy (MeV)	Cross section (mbarn) Rudstam	ALICE
800 - 700	6.48	-
700 - 600	6.47	-
600 - 500	6.36	-
500 - 400	6.08	-
400 - 300	5.48	-
300 - 200	4.62	-
200 - 100	4.3	18.2
100 - 50	1.52	19.9
50 - 25	0.118	5.83×10^{-3}
25 - 20	2.54×10^{-3}	0
20 - 17	3.72×10^{-4}	0
17 - 15	7.2×10^{-5}	0

Table C.10: Group cross sections of the reaction $Cu_{nat}(n,x)^{52}Mn$

Energy (MeV)	Cross section (mbarn) Rudstam	ALICE
800 - 700	6.88	-
700 - 600	6.48	-
600 - 500	5.91	-
500 - 400	5.09	-
400 - 300	3.93	-
300 - 200	2.54	-
200 - 100	1.39	15.7
100 - 50	0.177	2.56
50 - 25	3.24×10^{-3}	0
25 - 20	3.68×10^{-6}	0
20 - 17	1.58×10^{-7}	0
17 - 15	1.08×10^{-8}	0

Table C.11: Group cross sections of the reaction $Cu_{nat}(n,x)^{54}Mn$

Energy (MeV)	Cross section (mbarn) Rudstam	ALICE
800 - 700	29.5	-
700 - 600	28.6	-
600 - 500	27.09	-
500 - 400	24.56	-
400 - 300	20.5	-
300 - 200	15.11	-
200 - 100	10.72	28.0
100 - 50	2.56	10.5
50 - 25	0.083	0.607
25 - 20	$4.22x10^{-4}$	0
20 - 17	$3.35x10^{-5}$	0
17 - 15	$3.88x10^{-6}$	0

Table C.12: Group cross sections of the reaction $Cu_{nat}(n,x)^{48}V$

Energy (MeV)	Cross section (mbarn) Rudstam	ALICE
800 - 700	6.76	-
700 - 600	6.02	-
600 - 500	5.09	-
500 - 400	3.95	-
400 - 300	2.62	-
300 - 200	1.31	-
200 - 100	0.438	6.82
100 - 50	0.022	$2.58x10^{-2}$
50 - 25	$9.16x10^{-5}$	0
25 - 20	$5.32x10^{-9}$	0
20 - 17	$6.58x10^{-11}$	0
17 - 15	$1.6\ x10^{-12}$	

Table C.13: Group cross sections based on experimental results (Michel /15/) of the reaction $^{59}Co(n,x)^{55}Co$

Energy (MeV)	Cross section (mbarn)
800 - 200	2.7
200 - 100	3.2
100 - 50	4.9
50 - 25	0.1
25 - 20	0
20 - 17	0
17 - 15	0

Table C.14: Group cross sections based on experimental results (Michel /15/) of the reaction $^{59}Co(n,x)^{56}Co$

Energy (MeV)	Cross section (mbarn)
800 - 200	13.8
200 - 100	18.8
100 - 50	42.2
50 - 25	19.6
25 - 20	0
20 - 17	0
17 - 15	0

Table C.15: Group cross sections based on experimental results (Michel /15/) of the reaction $^{59}Co(n,x)^{58}Co$

Energy (MeV)	Cross section
800 - 200	59.8
200 - 100	79.1
100 - 50	141.5
50 - 25	269.2
25 - 20	540.7
20 - 17	500.4
17 - 15	290.9

Table C.16: Group cross sections based on experimental results (Michel /15/) of the reaction $Ni(n,x)^{56}Ni$

Energy (MeV)	Cross section (mbarn)
800 - 200	3.1
200 - 100	3.8
100 - 50	6.6
50 - 25	7.6
25 - 20	0.6
20 - 17	0.1
17 - 15	0

XII. APPENDIX D

Comparison of Cross Sections for Proton Induced Reactions on Copper

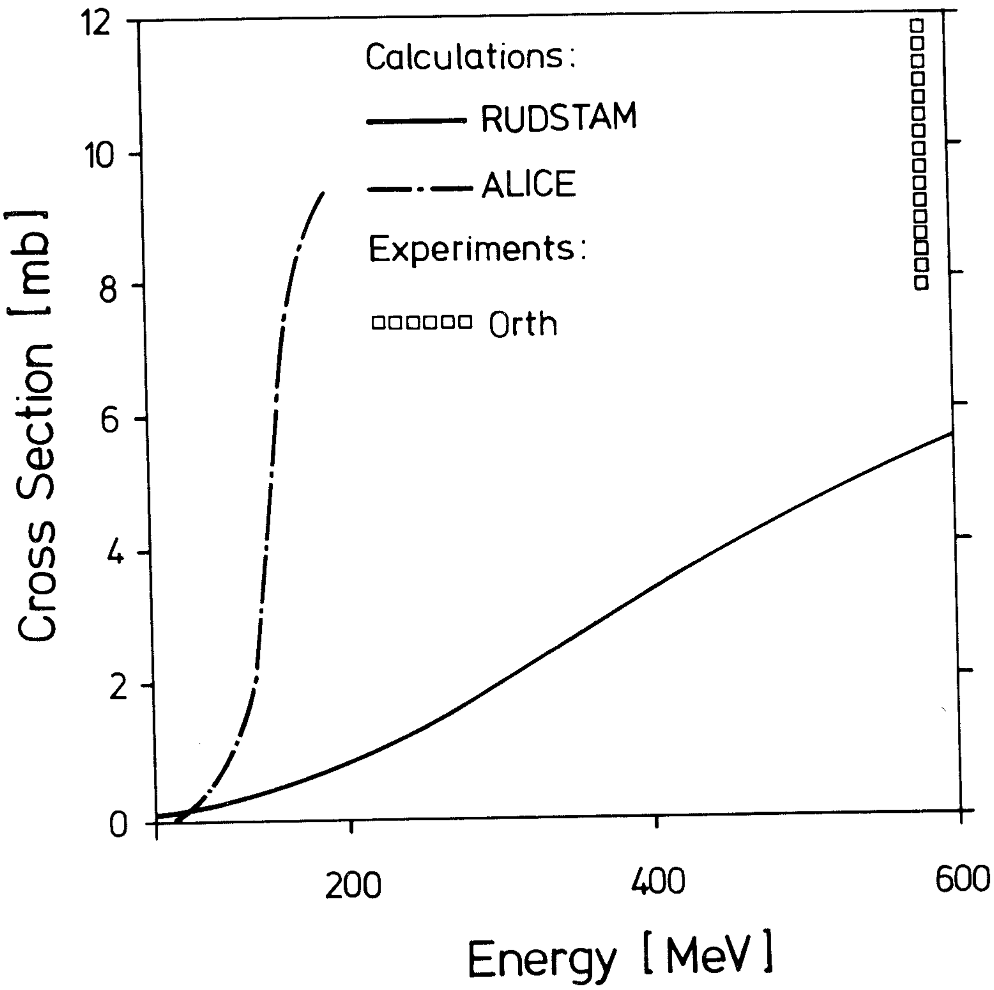

Fig. D.1 Experimental cross sections /11-14/ and model calculations /8,9/ for the production of ^{48}V from copper

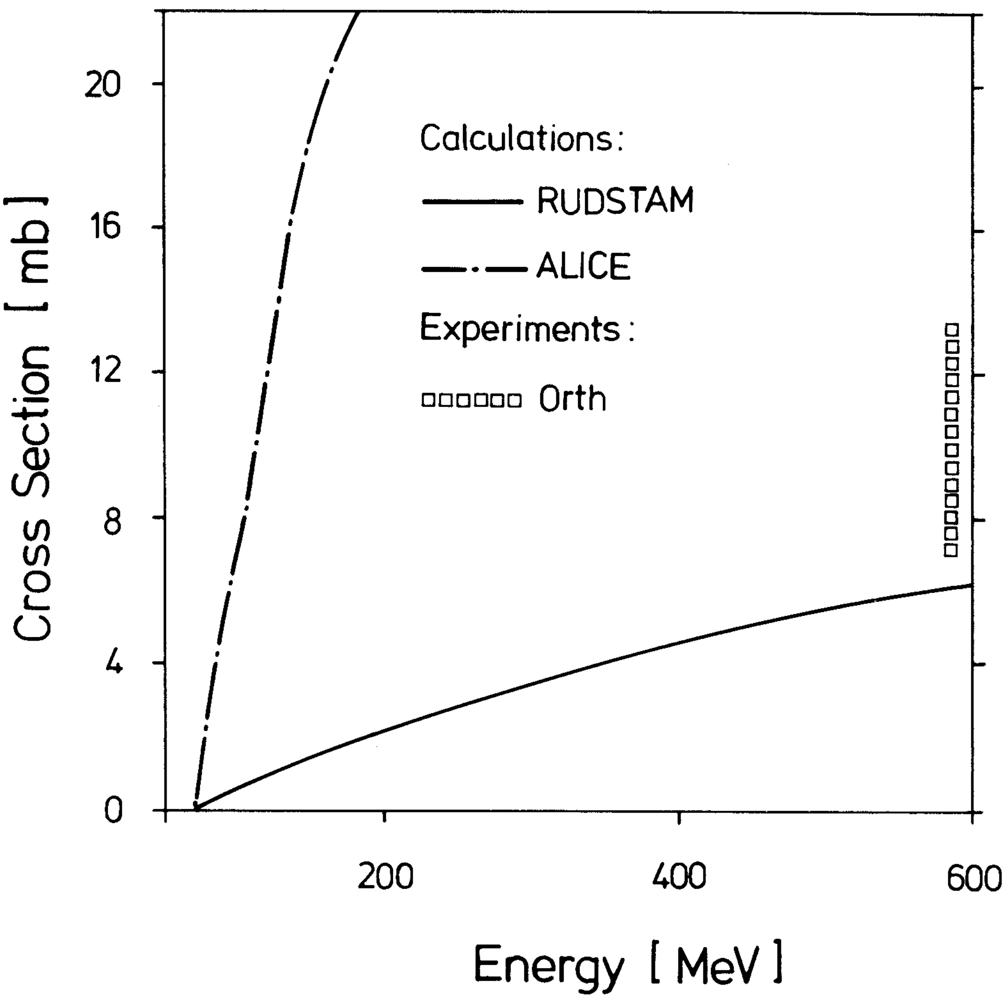

Fig. D.2 Experimental cross sections /11-14/ and model calculations /8,9/ for the production of ^{52}Mn from copper

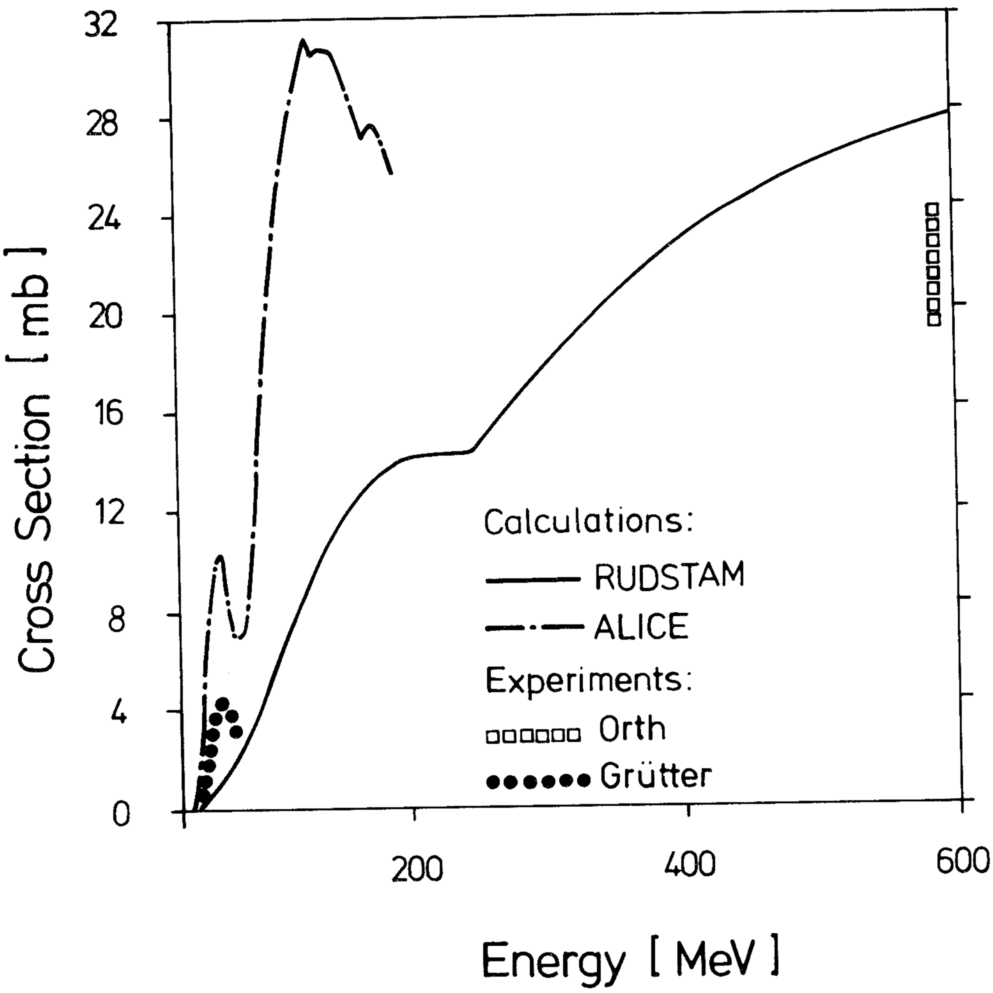

Fig. D.3 Experimental cross sections /11-14/ and model calculations /8,9/ for the production of ^{54}Mn from copper

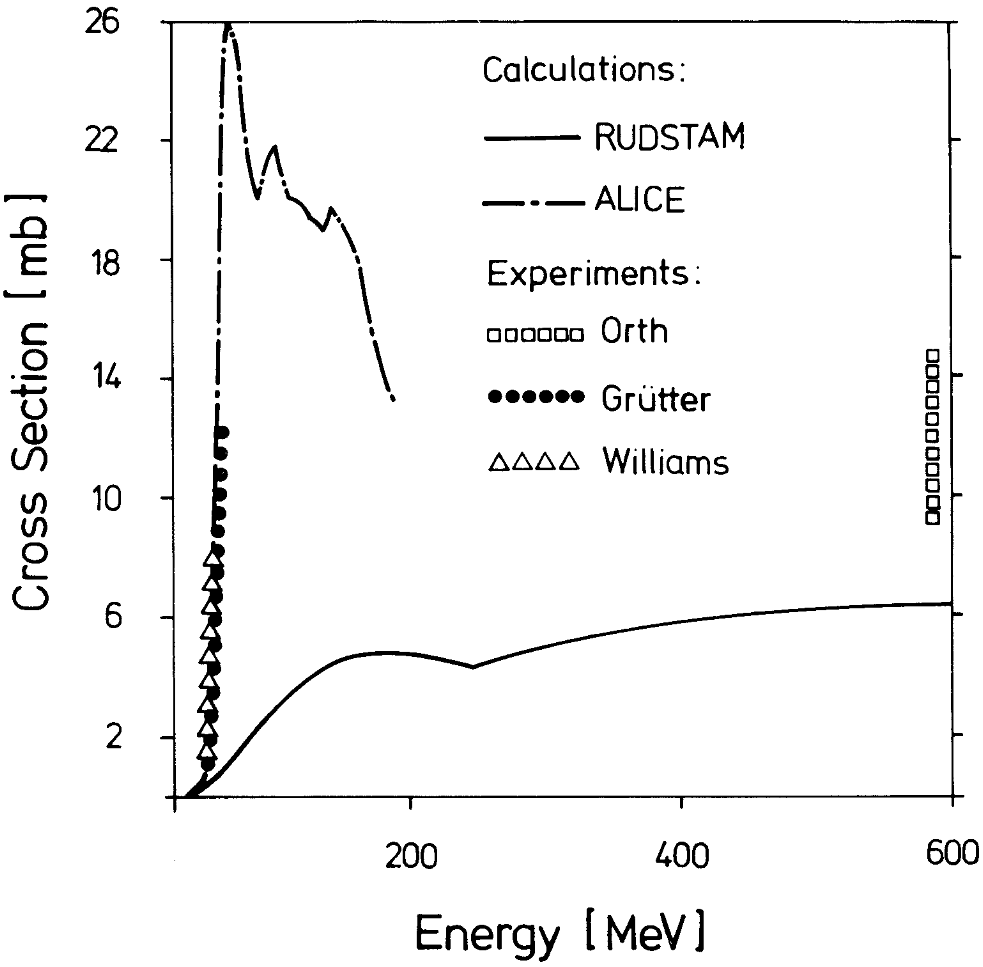

Fig. D.4 Experimental cross sections /11-14/ and model calculations /8,9/ for the production of ^{56}Co from copper